Materials Science & Engineering B xxx (xxxx) 115954

Contents lists available at ScienceDirect

Materials Science & Engineering B

journal homepage: www.elsevier.com/locate/mseb

Structural evolution and electrical conductivity of Ti_3C_2-SiOC ceramics

Sanjay Kumar Devendhar Singh, Kathy Lu *

Department of Materials Science and Engineering, Virginia Polytechnic Institute and State University, Blacksburg, VA 24061, USA

ARTICLE INFO

Keywords:
Ti_3C_2
Exfoliation
Surface functionalization
SiOC
Electrical conductivity

ABSTRACT

In this study, MXene Ti_3C_2 has been exfoliated and functionalized and then for the first time dispersed into polysiloxane (PSO) to produce Ti_3C_2-SiOC ceramics after 1000 °C pyrolysis. The pyrolyzed Ti_3C_2-SiOC is comprised of a network of amorphous SiOC dispersed with Ti_3C_2 and carbon. The conductivity in the pure SiOC matrix occurs through free carbon while the Ti_3C_2-SiOC composite exhibits enhanced charge transport due to increased percolation pathways from Ti_3C_2. Two-conductivity regimes are observed for both the pure SiOC and the Ti_3C_2-SiOC composite: band tail hopping conduction (BTH) mechanism below 400 °C and Arrhenius mechanism above 400 °C. Increasing the measurement temperature results in increased electrical conductivity. There is a two-pathway mechanism for the pure SiOC matrix but a single percolation pathway mechanism for the Ti_3C_2-SiOC composite. This work provides a new series of Ti_3C_2-SiOC ceramics and fundamental understanding of their electrical properties from room temperature to 1000 °C.

1. Introduction

Search for new inorganic 2D materials led to the discovery of MXenes [1–4]. Among these 2D materials, the most recognized species is Ti_3C_2. Recent work showed that calcination temperature improves the electrical conductivity; for untreated Ti_3C_2, the electrical conductivity can reach 850 $S{\cdot}cm^{-1}$ while for those calcined at 400 and 600 °C the conductivity values are 1430 $S{\cdot}cm^{-1}$ and 2410 $S{\cdot}cm^{-1}$, respectively [5]. Functionalization of Ti_3C_2 with suitable moieties would open a wide range of possibilities to create materials with claylike behaviors or interesting optical, thermal, and electrical properties. For example, the transparency of spin-cast thin films of Ti_3C_2 can be modified by intercalation of moieties (e.g., hydrazine, NH_4HF_2, or Na^+ ions); the resulting materials can be used for transparent electrodes [2,6].

Polymer derived ceramics (PDCs) are being studied for gas storage [7], catalysis [8], electrodes [9], among others [10–17,18,19,20]. SiOC systems are the most widely studied PDCs for different applications. The electrical conductivity of SiOCs strongly depends on carbon content [21,22]. Below the carbon percolation threshold, the electrical conductivity is mainly related to the properties of the SiOC matrix [22]. Above the carbon percolation threshold, the electrical conductivity is mainly determined by the carbon phase structure and distribution [22,23]. Therefore, the amount and phase of carbon in the SiOC matrix have great influence on the electrical conductivity. Polycarbosilane pyrolyzed at 1000 °C in an Ar atmosphere was comprised of amorphous SiOC and SiC nanodomains with an electrical conductivity on the order of 10^{-10} $S{\cdot}cm^{-1}$ [24]. The low electrical conductivity could be due to either low mobility or low concentration of charge carriers [24]. SiOC ceramics derived from polyhydromethylsiloxane and divinylbenzene mixtures (pyrolyzed at 1400 °C in Ar) showed an electrical conductivity of 2.58 $S{\cdot}cm^{-1}$ and 4.28 $S{\cdot}cm^{-1}$ at room temperature and 400 °C, respectively [25]. For SiOC ceramics derived from different polymer precursors [26], the electrical conductivity changes with the pyrolyzing temperature and the polymer precursors [26]. Mixtures containing polyhydromethylsiloxane and vinyl-terminated polyphenylmethylsiloxane exhibited an electrical conductivity of 6.64 $S{\cdot}cm^{-1}$ (pyrolyzed at 1300 °C) and 7.05 $S{\cdot}cm^{-1}$ (pyrolyzed at 1400 °C) at 303 °C and 403 °C respectively [26], while that containing polyhydromethylsiloxane and polydimethylsiloxane revealed a conductivity of 2.34 $S{\cdot}cm^{-1}$ at 415 °C (pyrolyzed at 1400 °C) [26]. TiC_xO_y-containing SiOC had an electrical conductivity of 5.03 $S{\cdot}cm^{-1}$ at 400 °C [27]. To obtain high electrical conductivity, highly conductive additives need to be considered.

Since Ti_3C_2 is highly conductive and fundamentally a ceramic material, it has the great potential to enhance the electrical conductivity when properly introduced into the SiOC matrix [25,27]. Care should be taken to achieve a homogeneous distribution of Ti_3C_2 layers in the SiOC matrix while not changing the property of Ti_3C_2 during the high temperature pyrolysis process. Pure Ti_3C_2 heated in argon to 1000 °C was stable with a minor weight loss of ~ 2.47 % at 800 °C [28]. However, after 1000 °C, Ti_3C_2 reacted with the O_2 impurity in Ar and formed a

* Corresponding author.
E-mail address: klu@vt.edu (K. Lu).

https://doi.org/10.1016/j.mseb.2022.115954
Received 4 September 2021; Received in revised form 26 June 2022; Accepted 13 August 2022
0921-5107/© 20XX

weak rutile TiO_2 structure [28]. Recently, classical molecular dynamics simulations predicted that the thermal degradation temperature for Ti_3C_2 is ~ 1227 °C [29], above which Ti_3C_2 undergoes changes in its crystal structure due to thermal disorder [29]. Therefore, pyrolysis of PSO dispersed with Ti_3C_2 in an argon atmosphere at a suitable temperature has the great potential for the formation of SiOC plus carbon with embedded planar Ti_3C_2. Relying on the charge carrier contribution from the planar Ti_3C_2, the electrical conductivity of the Ti_3C_2-SiOC composites can be greatly enhanced.

In this study, exfoliated Ti_3C_2 was functionalized using an APTES solution, followed by thermal analysis using thermogravimetry (TGA). The bonding characteristics were examined using Raman and FT-IR spectroscopies while the phases were analyzed using X-ray diffraction (XRD). The functionalized Ti_3C_2 was for the first time dispersed in PSO and pyrolyzed in an Ar atmosphere to yield Ti_3C_2-SiOC ceramics at 1000 °C, for which both four-point probe DC measurement and electrochemical impedance spectroscopy (EIS) were used to measure the electrical conductivity from room temperature to 1000 °C. The electrical conductivity mechanisms for different Ti_3C_2-SiOC ceramics were discussed.

2. Experimental procedures

2.1. Materials

$Ti_3C_2T_x$ and TBAOH (54–56 wt% in H_2O) were purchased from XFNano Materials Tech. Co., ltd., China and Sigma-Aldrich, USA respectively. Polysiloxane (PSO; SPR-684; Starfire Systems, Inc., [-$Si(C_5H_6)_2O$–)$_3$(-$Si(CH_3)(H)O$-)$_2$(-$Si(CH_3)(CH=CH_2)O$-)$_2$]) and 2.1–2.4 % platinum divinyltetramethyldisiloxane complex in xylene (as the catalyst) were supplied by Gelest Inc. PA. DMSO of 99.99 % purity was supplied by Fisher Scientific Company, NJ.

2.2. Exfoliation and surface functionalization of Ti_3C_2

Ti_3C_2 was exfoliated using TBAOH and DMSO. Initially a solution containing 75 wt% TBAOH in a DMSO solvent was prepared by stirring the solution at room temperature for 30 min. Subsequently, these solutions were diluted to 30 mL using hexane at room temperature. 30 mL of such a solution was added dropwise to 4.12 wt% (relative to TBAOH and DMSO weight) $Ti_3C_2T_x$ with stirring (500 rpm) at 30 °C for 48 h to remove residual gases (e.g., NH_3). Subsequently, the mixture was ultrasonicated for 2 h at 30 °C. The derived mixtures were then centrifuged at 3200 rpm for 30 min. The supernatant liquid was decanted and used for studies while the sediment was used for further exfoliation.

The derived Ti_3C_2 solution was mixed slowly with 2.0–2.5 wt% APTES solution dropwise. Addition of APTES to the Ti_3C_2 solution resulted in instantaneous heat release. Therefore, mixing was first carried out in an ice cold condition to avert any undesirable reactions. Then, the mixtures were stirred at 1000 rpm at room temperature for 48 h in order to fully functionalize Ti_3C_2.

The amount of Ti_3C_2 loaded in PSO was calculated using Digimat software. The thickness of the exfoliated Ti_3C_2 layers was assumed as 2 nm while their length and width were varied between 0.5 and 7 μm [30,31]. 3D Representative Volume Elements (RVEs) of Ti_3C_2 in the SiOC matrix were generated using the Digimat-FE module. Mechanical properties for SiOC, such as Young's modulus (101 ± 15 GPa) [32], density (1.90 g·cm^{-3}) [12], and Poisson's ratio (0.11) [32], were used to derive 3D RVEs during the Digimat-FE modelling. While interpenetration of Ti_3C_2 layers was prohibited for realistic filling/packing in a given cube, no mechanical properties for Ti_3C_2 were required in Digimat.

2.3. Preparation of Ti_3C_2-SiOC

In a typical experiment, a certain quantity of APTES functionalized Ti_3C_2 was mixed with PSO (in wt% relative to that of PSO). To this mixture, 10 ppm of Pt catalyst (relative to PSO) was added and stirred for 3 h at 30 °C. Subsequently, the mixture was degassed in a vacuum chamber (10 mTorr) for 2 h and poured into cylindrical aluminum foil molds. The mixture was then placed in vacuum for 10 min to remove residual bubbles and kept in an oven for 12 h at 60 °C, then at 120 °C for 24 h, and then at 150 °C for 12 h respectively. The cured samples were polished and ultrasonicated in ethanol for 30 min, and then polished on both sides before their dimensions were measured. In order to yield defect-free samples after pyrolysis, each sample was covered by graphite felts and well separated during pyrolysis in a tube furnace (1730–20 Horizontal Tube Furnace, CM Furnaces Inc., Bloomfield, NJ) with an Ar gas flow of 900 mL·min^{-1} up to 1000 °C. The heating rate was 2 °C·min^{-1} and the holding time at this temperature was 2 h. The product after pyrolysis was cylindrical discs of ~ 12 mm diameter and ~ 3 mm height. These samples were intact, dense, and crack-free.

2.4. Characterization

The bonding characteristics of the crosslinked samples were measured using FT-IR spectroscopy (Niolet 8700 with a Pike GladiATR attachment, Thermo Scientific, Waltham, MA). Raman spectroscopy was carried out at 532 nm excitation using a Horiba spectrometer (JY, Horiba HR 800). Thermogravimetric analysis (TGA) was carried out in an Ar atmosphere at 10 °C·min^{-1} heating rate until 1000 °C (STA 449 Jupiter® Analyzer, NETZSCH-Geratebau GmbH, Germany). The densities of the pyrolyzed samples were measured using the Archimedes method with water as the immersion medium. The phase characterization of the pyrolyzed samples and Ti_3C_2 was carried out using an X'Pert PRO diffractometer (PANalytical B.V., EA Almelo). The electrical conductivity of the pyrolyzed samples was carried out by using VerSTAT 3 from Princeton Applied Research, Oak Ridge, TN in a four-point probe configuration from room temperature to 1000 °C and in a flowing Ar atmosphere. The morphologies of Ti_3C_2 were examined using scanning electron microscopy (SEM, Quanta 600 FEG, FEI, Hillsboro, OR) after the samples were coated with Au-Pd up to a thickness of 5.5 nm using a Leica EM ACE600 sputter.

3. Results and discussion

3.1. Exfoliation and functionalization of Ti_3C_2

TBAOH ($(C_4H_9)_4NOH$) comprises bulky -C_4H_9 groups, which upon intercalation exert excess strain on the layered Ti_3C_2 and cause it to exfoliate. The exfoliated Ti_3C_2 is generally 2D layered. However, the thickness of the exfoliated Ti_3C_2 layers depends on the penetration ability of TBAOH. On the other hand, DMSO has a dual function: aiding TBAOH to penetrate in-between the Ti_3C_2 layers and dispersing the exfoliated Ti_3C_2 (with a very small thickness) to form a stable colloidal solution. Exfoliated Ti_3C_2 layers need to be free from TBAOH and DMSO afterwards. Presence of either one can result in agglomeration of the Ti_3C_2 layers when dispersed in the PSO polymer liquid.

The FT-IR spectra for Ti_3C_2, TBAOH, and APTES are shown in Fig. 1. The surface of exfoliated Ti_3C_2 is comprised of terminal bonds of –OH, =O, and –F. Theoretically, the IR vibrational mode due to $Ti_3C_2(OH)_2$ arises at ~ 3732 cm^{-1} and between 244 and 637 cm^{-1} [33]. The IR vibrational modes for $Ti_3C_2O_2$ and $Ti_3C_2F_2$ arise in the range of 179 to 675 cm^{-1} [33]. In this study, the delaminated Ti_3C_2 layers were dried in butane (C_4H_{10}) before the FT-IR analysis and were baseline corrected in order to examine the observed modes of vibration (inset in Fig. 1). The minor vibrational mode at 3325 cm^{-1} confirms the presence of –OH bonds, consistent with [33,34] while the –Ti = O vibrational mode is

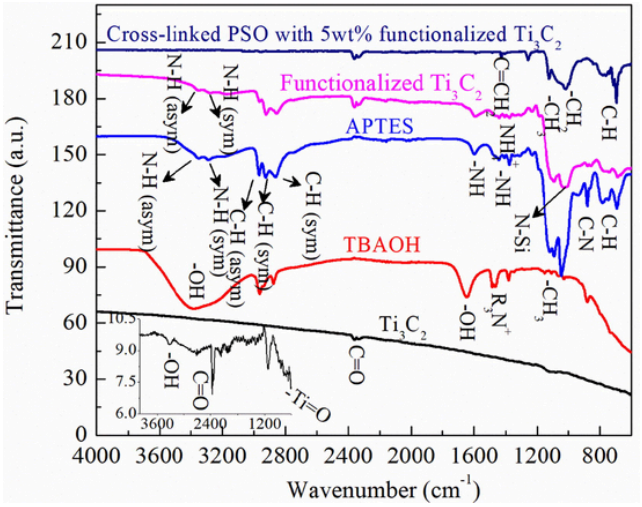

Fig. 1. Bonding characteristics of the exfoliated Ti_3C_2, TBAOH, APTES, functionalized Ti_3C_2, and cross-linked PSO with 5 wt% Ti_3C_2 at room temperature. The inset shows the baseline corrected FT-IR spectra of Ti_3C_2.

exhibited at 661 cm^{-1}. The vibrational modes due to –Ti-F could not be assigned due to the instrument detection limit. TBAOH shows strong asymmetric and symmetric C—H stretching vibrational modes due to $–CH_3$ at 2963 and 2937 cm^{-1}. A strong broad peak centered around 3352 cm^{-1} is due to the presence of hydroxyl groups in TBAOH. For pure APTES, two minor peaks appearing at 3351 and 3294 cm^{-1} are due to asymmetric and symmetric stretching of N—H of NH_2. The bands at 2974, 2928, and 2885 cm^{-1} are attributed to C—H stretching of CH_3 (asymmetric), CH_2 (asymmetric), and CH_3 (symmetric) vibrational modes respectively. The NH_2 bending vibrational band appears in the 1610–1580 cm^{-1} region. The C—N stretching appears in the range of 1250–1020 cm^{-1} while a sharp out-of-plane bending peak of C—N appears at 881 cm^{-1}.

The terminal bonds –OH, =O, and –F on Ti_3C_2 can be used for functionalization by exploiting the electropositive groups present in APTES, –Si-O and $–NH_2$. The two species undergo either condensation and/or hydrogen bonding. Fig. 1 shows the FT-IR spectra of Ti_3C_2 functionalized with APTES. The functionalized Ti_3C_2 exhibits the bonding fingerprints characteristic of $[Ti_3C_2(APTES)_2]$. Since the exfoliated Ti_3C_2 layers were washed completely before being functionalized with APTES, the vibrational modes observed in functionalized Ti_3C_2 due to C—H stretching were observed at 2965, 2920, and 2885 cm^{-1}. These vibrational modes are attributed to $–CH_3$ (asymmetric), $–CH_2$ (asymmetric), and $–CH_3$ (symmetric) vibrations in APTES. The observed wavenumbers for $–CH_3$ (asymmetric), $–CH_2$ (asymmetric), and $–CH_3$ (symmetric) vibrations are in-line with those for the pure APTES ($–CH_3$ and $–CH_2$ modes). The very low intensity peaks appearing at 3351 and 3294 cm^{-1} are ascribed to the presence of residual, unreacted $–NH_2$ groups, resulting in N—H asymmetric and symmetric stretching modes of vibration. Further, the intensity, peak splitting, and range are different from TBAOH; the vibrational modes mirror that of pure APTES, which further confirms that these are due to APTES functionalization. The stretching vibrational mode observed at 2853 cm^{-1} is due to C—H symmetric stretching of $–CH_2$ groups. The weak bands appearing at 1454 and 1388 cm^{-1} are due to ammonium ions. The TBAOH absorption bands between 1200 and 600 cm^{-1} are absent, indicating that no TBAOH is present in the APTES functionalized Ti_3C_2 sample. The condensation reaction between APTES and Ti_3C_2 results in a characteristic change from N—H to N-Si with a broad peak centered around 1019 cm^{-1} [35]. Additionally, a broad peak appears between 650 and 950 cm^{-1}, which is characteristic of secondary amine. The –OH peaks at 1100, 1055, 1020, and 990 cm^{-1} are due to the stretching vibrations of C-OH groups. The characteristic peaks observed between 1163 and 635 cm^{-1} are suppressed and broad, which should be due to the interaction between Ti_3C_2 and APTES, resulting in changes in their vibrational frequency modes. For the crosslinked PSO with functionalized Ti_3C_2 (Fig. 1, the PSO sample has a high Ti_3C_2 amount in order to observe the transmittance peak), the C—H vibrational modes corresponding to $–CH_3$, $–CH_2$, and phenyl groups of the cross-linked polymer can be observed between 1160 and 700 cm^{-1}. The low intensity peak observed at 2342 cm^{-1} is attributed to stretching vibration due to surface adsorbed O=C = O. The cross-linked PSO-Ti_3C_2 shows the characteristic vibrations of PSO from 1100 to 1000 cm^{-1}. The vibrational mode observed at 1405 cm^{-1} is attributed to the presence of residual alkenes. The main advantage is that APTES helps to disperse the functionalized Ti_3C_2 in the polysiloxane matrix and prevents the segregation/agglomeration of Ti_3C_2.

Fig. 2 shows the Raman spectra of the pure Ti_3C_2 and pyrolyzed Ti_3C_2-SiOC samples at different Ti_3C_2 levels. Ti_3C_2 has 5 atoms in its primitive cell, therefore giving rise to 12 optical modes (Eqn. 1) and 3 acoustic modes of vibrations [33].

Ti_3C_2 (optical) = $4E_g$ (Raman) + $2A_{1g}$ (Raman) + $4E_u$ (IR) + $2A_{2u}$ (Raman) (1).

Depending on the terminal bonds present, the optical modes change (e.g., 18 for $Ti_3C_2O_2$ and 24 for $Ti_3C_2(OH)_2$) [36]. The Ti_3C_2 monolayers exhibit the atomic position of Ti1 (Ti1-C) and Ti2 (Ti2-C) at 2a (0, 0, 0.5) and 2d (1/3, 2/3, 0.6221) respectively [5]. The terminal atom weakens the in-plane vibration of C and Ti2 atoms. The strong Raman peak appearing at 152 cm^{-1} corresponds to the E_g mode. Additionally, the Raman peaks at 206 and 258 cm^{-1} correspond to the A_{1g} vibrational modes of $Ti_3C_2O_2$ and $Ti_3C_2(OH)_2$ respectively. The peak appearing at 421 cm^{-1} corresponds to the E_g vibrations of C atoms with –OH terminal groups ($Ti_3C_2(OH)_2$). The E_g vibration corresponding to the C atoms of Ti_3C_2 with –OH termination appears at 613 cm^{-1}. These peaks are indicative of Ti_3C_2.

The Raman spectra of the pure SiOC, 0.01 wt% Ti_3C_2-SiOC, and 1.0 wt% Ti_3C_2-SiOC are also shown in Fig. 2. The presence of free carbon clusters (graphitic carbon) is confirmed by their characteristic bands of D, G, 2D, and D + D'. The D and G modes correspond to A_{1g} and E_{2g} symmetry (in-plane bond stretching of sp^2 carbon atoms) respectively [37,38]. In principle, the D mode is forbidden in an ideal graphite structure and only appears when graphite has a disordered structure [38,39]. D' is another disorder-induced vibrational band; however it differs from the D mode due to phonon generation [40], which is from Γ point and K point respectively [37,38,41]. In addition, the peaks of the D and G modes of SiOC shift with the Ti_3C_2 content increase. SiOC has the D and G bands at 1313 and 1606 cm^{-1} while 0.01 wt% Ti_3C_2-SiOC has the peaks centered around 1325 (D band) and

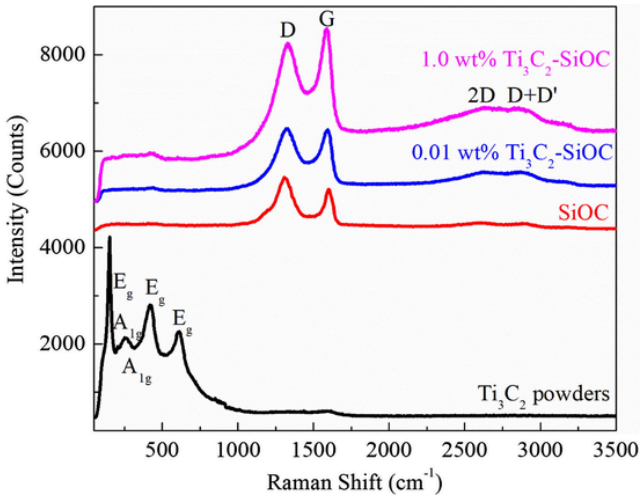

Fig. 2. Raman spectra of Ti_3C_2 and Ti_3C_2-SiOC composites.

1595 cm^{-1} (G band). Furthermore, 1.0 wt% Ti_3C_2-SiOC shows the corresponding peaks at 1330 and 1589 cm^{-1} respectively. The D band moves to higher wavenumbers while the G band shifts to lower wavenumbers. This could be due to the growth of carbon clusters in the presence of Ti_3C_2 or their higher cluster density in a given area. The peak integral of their corresponding D and G bands also increases with the Ti_3C_2 content, which confirms the graphitic carbon cluster size increase. The 2D and D + D' peaks also appear with the Ti_3C_2 content increase and are centered around 2641 and 2876 cm^{-1} respectively. The carbon cluster size for the pure SiOC, 0.01 wt% Ti_3C_2-SiOC, and 1.0 wt% Ti_3C_2-SiOC can be calculated as 1.60 nm, 1.77 nm, and 1.81 nm respectively [41]. The same method was used in our earlier work for carbon cluster size calculation and the results are consistent [42,43]. Therefore, Ti_3C_2 assists in carbon cluster growth.

Fig. 3 shows the XRD patterns of the exfoliated Ti_3C_2, pure SiOC, and Ti_3C_2-SiOC samples. Since XRD is not able to detect low concentrations of Ti_3C_2 in the SiOC matrix, a SiOC sample with 5 wt% Ti_3C_2 was prepared. For the pure Ti_3C_2 sample, the peaks are at 8.94°, 18.15°, 28.04°, and 60.80° respectively, originating from the diffractions of (0 0 2), (0 0 6), (0 0 8), (1 1 0) planes, consistent with earlier studies [12,13,44]. For the pure SiOC sample, the broad peak centered around 23° is from amorphous SiO_2 and the peak at 43° is from turbostratic carbon. For the Ti_3C_2-SiOC sample, the XRD halos and peaks are a combination of the SiOC and Ti_3C_2 species; the peaks corresponding to the (1 0 3), (1 0 7), (1 1 0), and (1 1 2) planes of Ti_3C_2 can be observed. This means that the Ti_3C_2 phase is preserved, indicating that the Ti_3C_2 phase is stable up to 1000 °C in the SiOC matrix.

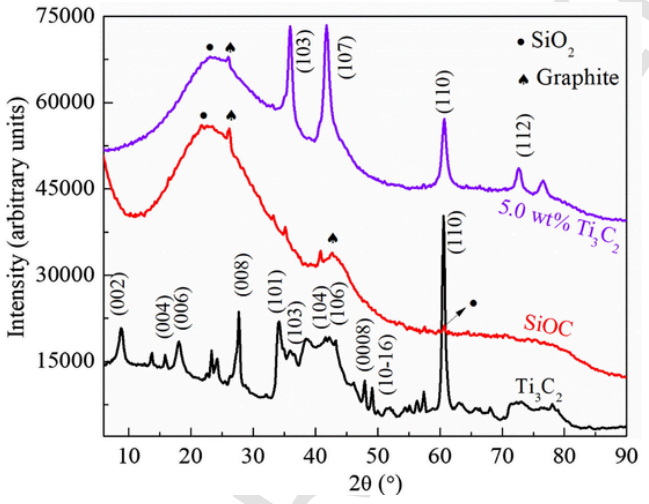

Fig. 3. XRD patterns of the exfoliated Ti_3C_2, pure SiOC, and 5.0 wt% Ti_3C_2-SiOC samples.

3.2. Ti_3C_2 morphology and dispersion

Fig. 4 shows the morphologies of Ti_3C_2 before and after exfoliation. The SEM image shows that the as-received Ti_3C_2 is agglomerated (Fig. 4a). The magnified image shows the layer structure (Fig. 4a inset). The exfoliated Ti_3C_2 is thin and transparent (Fig. 4b) and has a lateral size of a few microns to a few hundred nanometers while their thickness is about 2 nm.

To understand the concentration limit and size dependence of planar Ti_3C_2 in the SiOC matrix, the 3D Representative Volume Element (RVE) geometry was generated using Digimat-FE simulation. In a typical simulation run, the length, width, and thickness of Ti_3C_2 inclusions were fixed at Y × Y × 0.002 μm (where Y ranged between 7 and 0.5 μm). The volume of the simulation cube was fixed as 1000 μm^3. The Ti_3C_2 layer thickness was kept constant at 2 nm in all the Ti_3C_2 packing simulations. The simulation helped to calculate the weight percent of exfoliated Ti_3C_2 layers that could be accommodated in a SiOC matrix. During the Ti_3C_2 filling simulation, it was assumed that the exfoliated layers do not undergo any structural modifications such as folding and bonding between layers.

Table 1 shows the maximum number and weight percent of Ti_3C_2 layers for different given dimensions based on the Digimat-FE simulation. The underlying assumption is that the space in-between the Ti_3C_2 layers will be filled with PSO during crosslinking and then with SiOC after pyrolysis. The Ti_3C_2 layer packing takes place in a random 3D manner with no clustering/stacking. The simulated maximum weight percent ranges between 0.1 and 1.0 wt%. This range has been used as the guide to calculate the maximum content of Ti_3C_2 required to yield uniformly dispersed Ti_3C_2 in the SiOC matrix. As expected, larger size Ti_3C_2 2D layers lead to lower maximum packing weight percent of Ti_3C_2, which in turn reduces the weight fraction relative to that of the PSO matrix. Therefore, in the present work, the concentration of Ti_3C_2 is varied at 0, 0.05, 0.10, and 1 wt%, relative to that of PSO. In reality, both the Ti_3C_2 thickness and flake size vary. Table 1 serves as an approximate guide to estimate the maximum loading of exfoliated Ti_3C_2 in the PSO system.

Fig. 5 confirms that exfoliated Ti_3C_2 having smaller sizes can accommodate more Ti_3C_2 layers (5052 layers for 0.50 × 0.50 × 0.002 μm size in 1000 μm^3 volume) compared to that with larger sizes (only 152 layers for 7 × 7 × 0.002 μm size in 1000 μm^3 volume). The packing images for other Ti_3C_2 layer sizes are given in the supplement. Therefore, the dispersion and content of Ti_3C_2 in the SiOC matrix are related to the size of the Ti_3C_2 layers.

3.3. Ti_3C_2-SiOC pyrolysis behaviors

Table 2 shows the density, ceramic yield, and volume shrinkage of the pyrolyzed samples. The density of the pyrolyzed samples ranges from 1.84 ± 0.27 to 1.95 ± 0.31 $g{\cdot}cm^{-3}$. The theoretical densities of

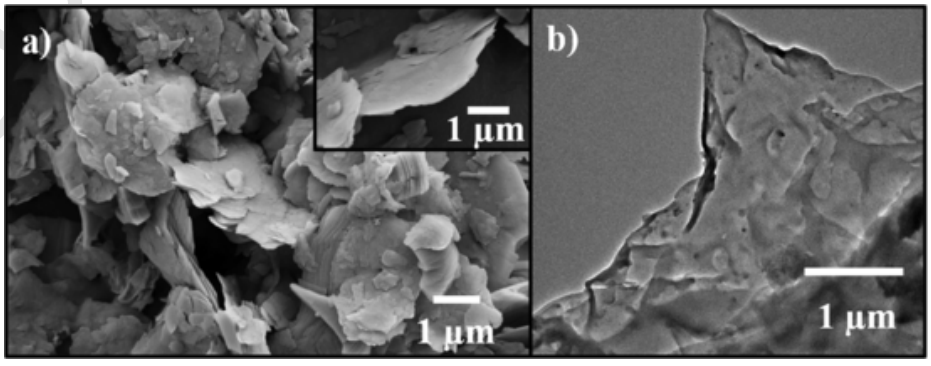

Fig. 4. a) Scanning electron image of as-received Ti_3C_2 without exfoliation, the inset shows the magnified image of a Ti_3C_2 layer; and b) transmission electron image of exfoliated and dispersed Ti_3C_2.

Table 1
Simulated maximum packing layers and weight percent of Ti_3C_2 with different sizes in a 1000 μm^3 cube using Digimat-FE simulation.

Size (μm)	Number of Ti_3C_2 layers	Weight percent (%)
7 × 7 × 0.002	152	0.10
6 × 6 × 0.002	216	0.11
5 × 5 × 0.002	356	0.12
4 × 4 × 0.002	701	0.15
3 × 3 × 0.002	756	0.16
2 × 2 × 0.002	1648	0.20
1 × 1 × 0.002	2752	0.63
0.75 × 0.75 × 0.002	3861	0.82
0.50 × 0.50 × 0.002	5056	1.00

the pure SiOC and Ti_3C_2 are 2.01 $g{\cdot}cm^{-3}$ and 5.2 $g{\cdot}cm^{-3}$, respectively. The Ti_3C_2-SiOC samples should have higher densities. However, due to the low concentration of Ti_3C_2, no significant change in their pyrolyzed density can be observed. The ceramic yield of the samples ranges between 77.11 ± 0.38 % and 80.07 ± 0.96 %. There is also no appreciable trend with increasing Ti_3C_2 content. Similarly, the shrinkage varies between 41.80 ± 3.05 % and 42.07 ± 2.11 %. Overall, no marked difference or trend is observed for the pyrolyzed density, shrinkage, or ceramic yield (Table 2).

Fig. 6 shows the weight change of the pure SiOC and 1 wt% Ti_3C_2-SiOC samples during pyrolysis in an Ar atmosphere. The maximum weight loss takes place between 300 °C and 600 °C. For the pure SiOC system, there are two weight loss peaks at 384.4 °C and 527.6 °C, respectively, which can be attributed to the break-up of the C—H, Si-C, and Si-O bonds in the SiOC system and hydrocarbon loss [12,15]. Such polymer decomposition and re-grouping lead to the formation of amorphous SiOC accompanied by the formation of Si-O, Si-C, and Si-H bonds [12,15]. These two thermal events occur simultaneously, therefore the weight loss peaks are continuous and overlapped. In general, the hydrocarbon-induced weight loss is high compared to that of depolymerization-induced weight loss. At ≥ 600 °C, the weight loss is gradual, with a transition point at 856.6 °C. The phase separation and atomic structural redistribution of Si-O, Si-C, and Si-C bonds at high pyrolysis temperatures do not involve gaseous species generation. For 1 wt% Ti_3C_2-SiOC, the weight loss is higher than that of the pure SiOC sample. Since Ti_3C_2 contains residual oxygen ($Ti_3C_2O_2$) (Fig. 2) and hydroxyl ($Ti_3C_2(OH)_2$) (Figs. 1 and 2) groups and is functionalized with APTES, these groups could have reacted with PSO during pyrolysis, leading to more release of CO_2, CO, and H_2O. As a result, the weight loss from the Ti_3C_2-SiOC sample is higher compared to that of SiOC. The initial weight loss for the Ti_3C_2-SiOC sample also starts earlier, at 298.9 °C, which could be due to the escape of the volatile species containing the solvent, H_2O, and surface adsorbed CO_2. The weight loss starting at 463.5 °C is due to polymer pyrolysis in the SiOC system and simultaneous loss of hydrocarbon species. The minor weight losses starting at 585.2 °C and 618.0 °C for PSO and 1 wt% Ti_3C_2-PSO, respectively, could be attributed to the restructuring of SiOC in addition to residual hydrocarbon weight loss.

3.4. Electrical conductivity

Fig. 7 shows the DC conductivity (σ) of the pure SiOC and different Ti_3C_2-SiOC samples from room temperature to 1000 °C in Ar. The conductivity increases exponentially with temperature. At lower temperatures (up to 400 °C), the electrical conductivity increases with the Ti_3C_2 content increase. For instance, the room temperature conductivity is highest for the 1 wt% Ti_3C_2-SiOC sample and the lowest for the pure SiOC ceramic. The increase in conductivity with 0.05, 0.1, and 1.0 wt% Ti_3C_2 is 16.7 %, 22.9 %, and 64.5 %, respectively. At high temperatures (from 400 °C to 1000 °C), the electrical conductivity continues to increase and largely overlaps for the pure SiOC and 0.05–0.1 wt% Ti_3C_2-SiOC samples, reaching the highest values of 5.01×10^{-2} $S{\cdot}cm^{-1}$ – 17.93×10^{-2} $S{\cdot}cm^{-1}$ at 1000 °C. The conductivity of the 1 wt% Ti_3C_2-SiOC sample, however, reaches the maximum of 5.40×10^{-2} $S{\cdot}cm^{-1}$ at 600 °C, above which there is a slight conductivity decrease. This is probably due to the surface oxidation of Ti_3C_2-SiOC and the reason for the observed phenomenon is elaborated below.

The amorphous SiOC matrix is known to have unpaired electrons due to a high number of dangling C bonds [45]. When the carbon content is low, the electrical conduction in such amorphous materials depends on localized states in the mobility gap and inherent defects [46,47] under thermal activation. When the amount of carbon clusters reaches a critical level, the conduction instead is determined by the carbon percolation [48]. Therefore, the conductivity mechanism in SiOC could be matrix-controlled conduction or percolation-controlled conduction. The specific conduction mechanism depends on the concentration of carbon clusters. Similarly, the electrical conductivity of SiOC with additives can demonstrate the percolation conduction mechanism when the additive amount is high enough.

The conductivity in amorphous carbon takes place via three mechanisms: conduction in extended states, conduction in band tails, and conduction in localized states at the Fermi levels. In this study, the DC electrical conductivity of Ti_3C_2-SiOC could be divided into two regimes: (a) room temperature to 400 °C and (b) from 400 °C to 1000 °C. These two regimes follow different mechanisms. Below 400 °C it follows the band tail hopping mechanism, which means that the logarithm of ohmic conductivity changes monotonically as a function of temperature [49].

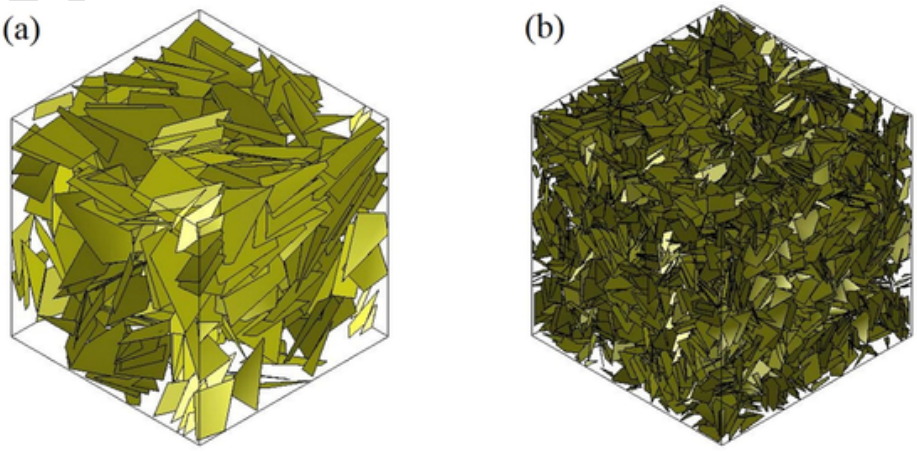

Fig. 5. Simulated packing characteristics of Ti_3C_2 sheets in polysiloxane derived from Digimat for Ti_3C_2 with length, width, and thickness of (a) 7 × 7 × 0.002 μm, (b) 0.5 × 0.5 × 0.002 μm.

Table 2
Pyrolyzed density, ceramic yield, and shrinkage of the SiOC and Ti_3C_2-SiOC samples.

wt% of Ti_3C_2	Pyrolyzed density (g·cm^{-3})	Ceramic yield (%)	Shrinkage (%)
0	1.92 ± 0.33	78.05 ± 0.26	41.99 ± 2.10
0.05	1.86 ± 0.44	79.39 ± 0.54	42.26 ± 2.17
0.10	1.84 ± 0.27	77.11 ± 0.38	41.80 ± 3.05
1.00	1.95 ± 0.31	80.07 ± 0.96	42.07 ± 2.11

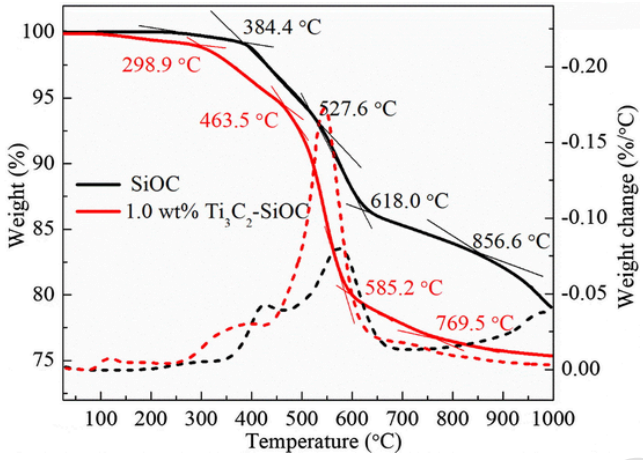

Fig. 6. Weight loss of the pure SiOC and Ti_3C_2-SiOC during pyrolysis in an Ar atmosphere.

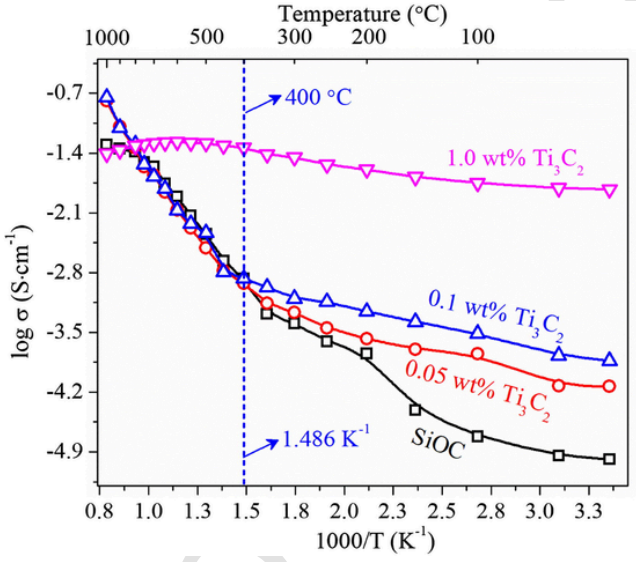

Fig. 7. DC conductivity as a function of temperature for the pure SiOC and Ti_3C_2 – SiOC samples. Each data point is the average of three measurements.

This theoretical description originates from the variable range hopping (VRH) process, which is dependent on $T^{-1/(d+1)}$, where d is hopping space dimensionality [50]. The VRH model is based on assumptions such as energy independence of density of states near the fermi level, neglecting correlations in a) the tunneling process, b) multiphoton processes, and c) electron phonon interactions. Therefore, the predicted values are lower than the experimental values when the conductivity is frequency dependent [49]. The modified band tail hopping conduction (BTH) is based on the filling rate of empty electronic orbitals and exponential tail state distribution [49]. In the BTH model, $T^{-0.25}$ is used as a result of dimensionality (d = 3) of the system under study. The conductivity result, logσ(T) as a function of $T^{-0.25}$ (Fig. 8), shows a good linear fit for both pure SiOC and Ti_3C_2-SiOC samples between room

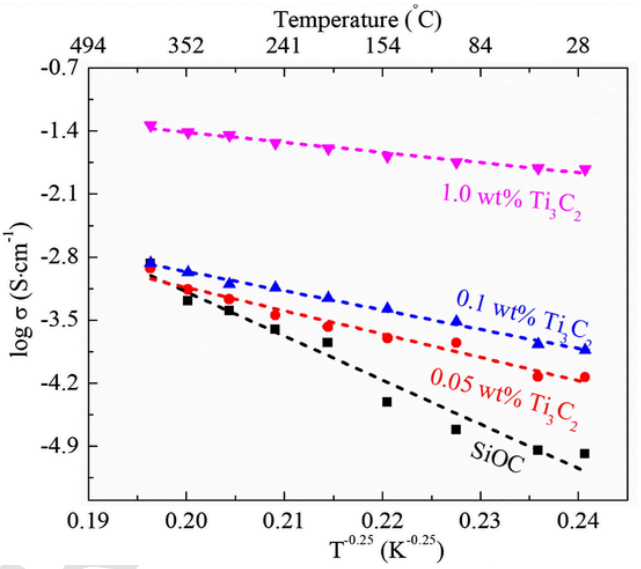

Fig. 8. Logσ(T) as a function of $T^{-0.25}$ between room temperature and 400 °C, showing linear relationships.

temperature and 400 °C. This means that below 400 °C, phonon assisted tunneling or hopping takes place in the SiOC and Ti_3C_2-SiOC samples. However, as the temperature increases to > 400 °C, the DC electrical conductivity shows an Arrhenius-like behavior; the charge carriers overcome the potential barrier by thermal activation; and high mobility carriers (electrons) are activated to the extended states [49]. The electrical conductivities of the pure SiOC and Ti_3C_2-SiOC (up to 0.1 wt% Ti_3C_2) samples increase with the Ti_3C_2 amount (Fig. 7). The activation energy (E_a) calculated using the Arrhenius equation (Eq. (2)) is 0.27 eV, 0.26 eV, and 0.25 eV respectively for the pure SiOC, 0.05 wt% Ti_3C_2-SiOC, and 0.1 wt% Ti_3C_2-SiOC samples. The decrease in the activation energy is likely due to the creation of more percolation pathways for the electrical conduction.

$$\sigma_c = \sigma_0 e^{-E_a/kT} \quad (2)$$

where σ_c and σ_0 are DC conductivity and pre-exponential factor respectively, T is absolute temperature, and *k* is Boltzmann constant.

Increasing measurement temperature from 400 °C to 1000 °C leads to continuous electrical conductivity increase. The electrical conductivities for the SiOC, 0.05 wt% Ti_3C_2-SiOC, 0.10 wt% Ti_3C_2-SiOC, and 1.0 wt% Ti_3C_2-SiOC at 400 °C are 1.34 × 10^{-3} S·cm^{-1}, 1.19 × 10^{-3} S·cm^{-1}, 1.33 × 10^{-3} S·cm^{-1}, and 4.62 × 10^{-2} S·cm^{-1}, respectively. The highest electrical conductivities for the SiOC, 0.05 wt% Ti_3C_2-SiOC, 0.10 wt% Ti_3C_2-SiOC, and 1.0 wt% Ti_3C_2-SiOC samples are 5.01 × 10^{-2} S·cm^{-1} (1000 °C), 15.80 × 10^{-2} S·cm^{-1} (1000 °C), 17.93 × 10^{-2} S·cm^{-1} (1000 °C), and 5.40 × 10^{-2} S·cm^{-1} (600 °C), respectively. The electrical conductivities of 0.05 wt% Ti_3C_2-SiOC and 0.10 wt% Ti_3C_2-SiOC converge as the temperature increases from 400 °C to 1000 °C, likely because the simultaneous temperature and electrical fields have destabilized the SiOC structure [25] and resulted in their microstructural changes. Increase in the Ti_3C_2 concentration in SiOC and simultaneous application of thermal and electric fields in Ti_3C_2-SiOC ceramics result in phase separation of SiOC to free carbon at the Ti_3C_2 interface (Fig. 2) along with surface oxidation of SiOC to SiO_2 and possible Ti_3C_2 oxidation. Therefore, their electrical conducting pathways are altered in this temperature range (400 °C – 1000 °C). Additionally, ordering of graphitic carbon could have happened [25], leading to the formation of a network of graphite-like lamellae of a few atomic layer size. The Raman spectra of Ti_3C_2-SiOC also show that exfoliated Ti_3C_2 has induced the formation of graphitic carbon and facilitated carbon cluster growth (Fig. 2). The measured carbon cluster size is 16.0 Å for SiOC, 17.8 Å for

0.01 wt% Ti_3C_2-SiOC, and 18.1 Å for 1.0 wt% Ti_3C_2-SiOC. However, the electrical conductivity of 1.0 wt% Ti_3C_2-SiOC decreases moderately with temperature between 600 °C and 1000 °C, even though the carbon cluster formation is more evident (Fig. 2). The plausible explanation is that simultaneous high temperature and electrical field might have induced the formation of oxide traces at the Ti_3C_2-SiOC interface and reduced the rate of charge carrier transport. At 1000 °C, 1.0 wt% Ti_3C_2-SiOC has an electrical conductivity of 43.06 × 10^{-2} S·cm^{-1} because of the thermal destabilization. However, compared to the other samples, 1.0 wt% Ti_3C_2-SiOC exhibits the highest electrical conductivity in the wide temperature range. Further, its activation energy is much lower at 0.12 eV. Therefore, the dominant charge carrier should be Ti_3C_2 and any oxidation of Ti_3C_2 would significantly affect the electrical conductivity.

Complex impedance spectra for the pure SiOC, 0.1 wt% Ti_3C_2-SiOC, and 1.0 wt% Ti_3C_2-SiOC samples from 1 Hz to 1 MHz are shown in Fig. 9. The data for the 0.05 wt% Ti_3C_2-SiOC sample are similar to those of the above Ti_3C_2-containing samples and thus omitted for brevity. The pure SiOC sample (Fig. 9a) shows two semi-circles, indicating the presence of two impedance mechanisms: conduction through the SiOC matrix and carbon clusters, similar to an earlier report [36]. The first semi-circle (the high frequency range or lower Z' values) represents the conduction through SiOC while the second semi-circle (the low frequency range or higher Z' values) shows the conduction via carbon clusters. Also, the Nyquist semi-circle areas, representing conduction through both the SiOC matrix phase and the carbon clusters, decrease with the measurement temperature. However, the semi-circles can only be observed up to 600 °C. At ≥ 600 °C measurement temperatures, the semi-circle disappears as shown in the Fig. 9(a) inset. This is due to the SiOC microstructure disruption and thus conductivity mechanism changes under the simultaneous electrical and thermal fields. In this case, the carbon cluster effect cannot be observed; and the ohmic resistance from the SiOC matrix is much lower with steep changes. The fundamental conduction mechanism is through electron jumping to the conduction band in the SiOC matrix.

An equivalent circuit can be constructed for the impedance data of the pure SiOC sample as shown in Fig. 10a in order to understand the SiOC conduction mechanism. The circuit of the SiOC phase and carbon clusters is in series and their corresponding resistor and capacitor components are in parallel. The impedance is due to the combined resistance of the SiOC matrix and carbon clusters. Since the capacitor is parallel to the resistor, the former acts as a short circuit and effectively removes the resistor component. In Fig. 9, at low frequencies (higher Z' values), the capacitor acts as an open circuit. Above a certain frequency, the impedance of the capacitor ($Z = -j/\omega C$) becomes smaller than the resistor (the SiOC matrix and carbon clusters). At high frequencies (lower Z' values), the impedance is entirely controlled by the interfacial ohmic resistance of SiOC and carbon clusters. Between 600 °C and 1000 °C, under the simultaneous electric and heating effects, the ohmic resistance of the pure SiOC is much lower, the electrical conduction is controlled by the electron jumping to the conduction energy band in the SiOC matrix (Fig. 7).

Fig. 9b-c show that the impedance spectra for all the Ti_3C_2-SiOC samples have one semi-circle. It has been reported that pure, unexfoliated Ti_3C_2 has an electrical conductivity of 2410 S·cm^{-1}. In this study, the room temperature electrical conductivity of SiOC is 1.03 × 10^{-5} S·cm^{-1} as shown in Fig. 7. The 0.05 wt% Ti_3C_2-SiOC, 0.10 wt% Ti_3C_2-SiOC, and 1.0 wt% Ti_3C_2-SiOC samples exhibit an electrical conductivity of 7.37 × 10^{-5} S·cm^{-1}, 1.47 × 10^{-4} S·cm^{-1}, and 1.50 × 10^{-2} S·cm^{-1}, respectively. Fig. 10b shows that the measured impedance plot matches well with the equivalent circuit for the 0.05 wt% Ti_3C_2-SiOC sample. The latter is comprised of an inductor and an ohmic resistor (R_Ω) due to Ti_3C_2, while the capacitor and polarization resistor (R_p) are due to the Ti_3C_2-SiOC interface. The inductor impedance (Ti_3C_2) increases with the frequency and Ti_3C_2 acts as a short circuit at low frequencies. The Ti_3C_2-SiOC-C interface comprises a capacitor and a resistor in parallel, which are in turn in series with Ti_3C_2. The capacitor (interface) impedance decreases with frequency increase while the resistor (ohmic resistance) is independent of the frequency. Since the capacitor impedance diminishes above a certain frequency and becomes much smaller than that of the resistor impedance (at the Ti_3C_2-SiOC-C

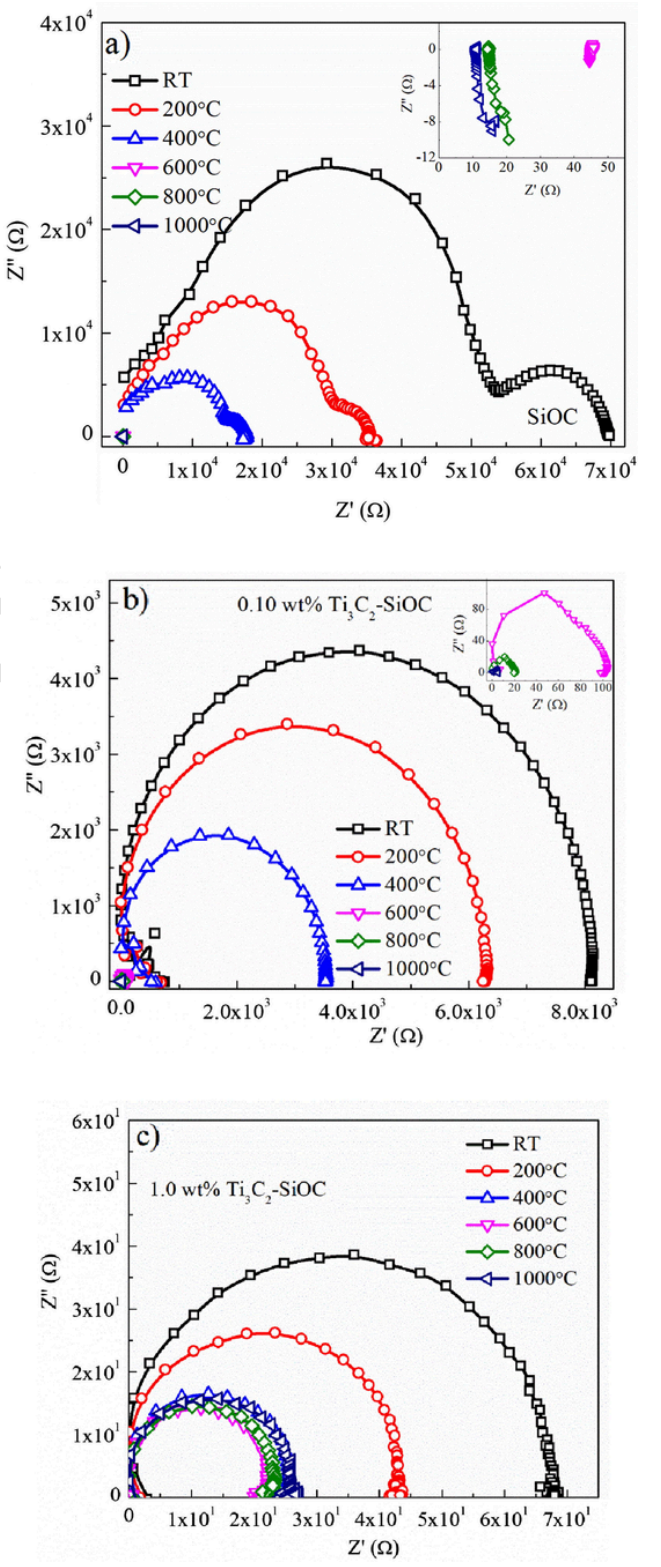

Fig. 9. Complex impedance spectra of a) pure SiOC, b) 0.1 wt% Ti_3C_2-SiOC, and c) 1.0 wt% Ti_3C_2-SiOC as a function of measurement temperature.

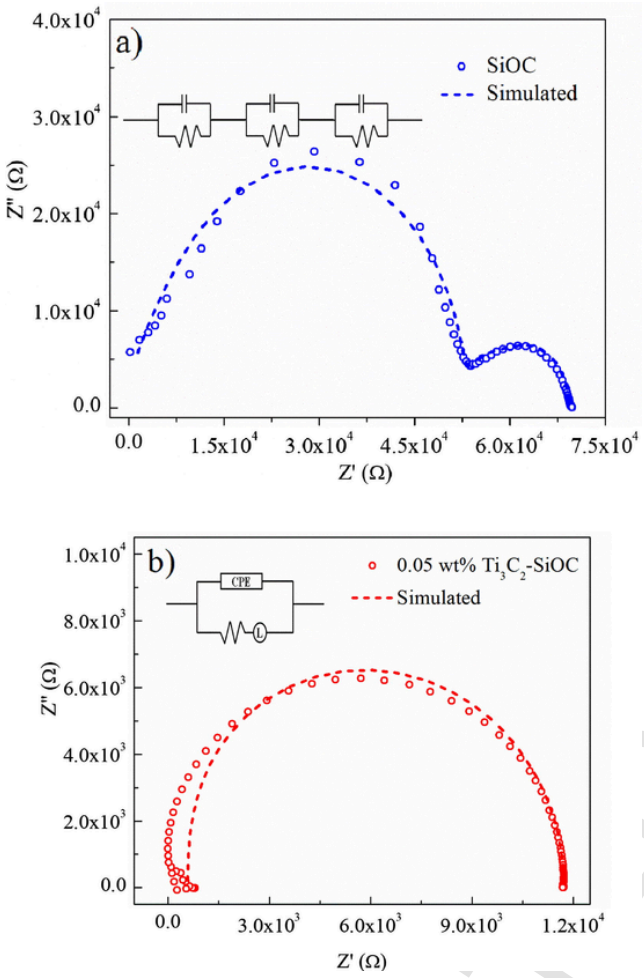

Fig. 10. Nyquist plot of the room temperature complex impedance spectra of a) SiOC and b) b) 0.05 wt% Ti_3C_2-SiOC along with simulated circuit results (dash line) and their corresponding electrical circuit diagrams.

interface), it acts as a short circuit and removes the resistor component from the circuit. At low frequencies, the capacitor acts as an open circuit and is effectively removed, its contribution to the electrical impedance is negligible. However, at high frequencies, the capacitor impedance becomes much smaller than the ohmic resistance. In all cases, the contribution of carbon conduction is minimal or negligible compared to that of the Ti_3C_2-SiOC-C interface or Ti_3C_2.

Similar equivalent circuit analysis can be carried out for 0.1 wt% Ti_3C_2-SiOC and 1.0 wt% Ti_3C_2-SiOC. The electron transport takes place via an inductor-resistor–capacitor mode in series for the Ti_3C_2-SiOC systems. The high frequency or low Z' semi-circle represents the ohmic resistance (R_Ω) while the low frequency range or high Z' semi-circle represents the resistance due to both the ohmic resistance (R_Ω) and polarization resistance (R_p). Therefore, the Ti_3C_2-SiOC samples only show one semi-circle and exhibit lower Z' compared to that of the pure SiOC system. As the concentration of Ti_3C_2 increases from 0.05 to 1.0 wt%, the semi-circle shifts towards the origin along with the size suppression (decrease in resistance). This further confirms that increase in the Ti_3C_2 concentration enhances the conduction with better percolation pathways. The disappearance of the conduction via the carbon clusters (right impedance semi-circle) also means that the polarization resistance of the SiOC and carbon clusters is negligible in the Ti_3C_2-SiOC samples. The major charge transport in Ti_3C_2-SiOC takes place via Ti_3C_2 or Ti_3C_2-SiOC-C interface while the contribution of the SiOC matrix is minimal. The high temperature electrical conductivity from 600 °C to 1000 °C is due to thermally activated jumping of electrons to the conduction energy band (ohmic resistance).

Fig. 11 shows the real impedance (Z') as a function of frequency for the SiOC, 0.10 wt% Ti_3C_2-SiOC, and 1.0 wt% Ti_3C_2-SiOC samples from room temperature to 1000 °C. The data for the 0.05 wt% Ti_3C_2-SiOC sample are similar to those for the other two Ti_3C_2-containing samples and thus omitted for brevity. In the low frequency range, the Z' difference is indicative of the ohmic resistance. Fig. 11a shows an inflection

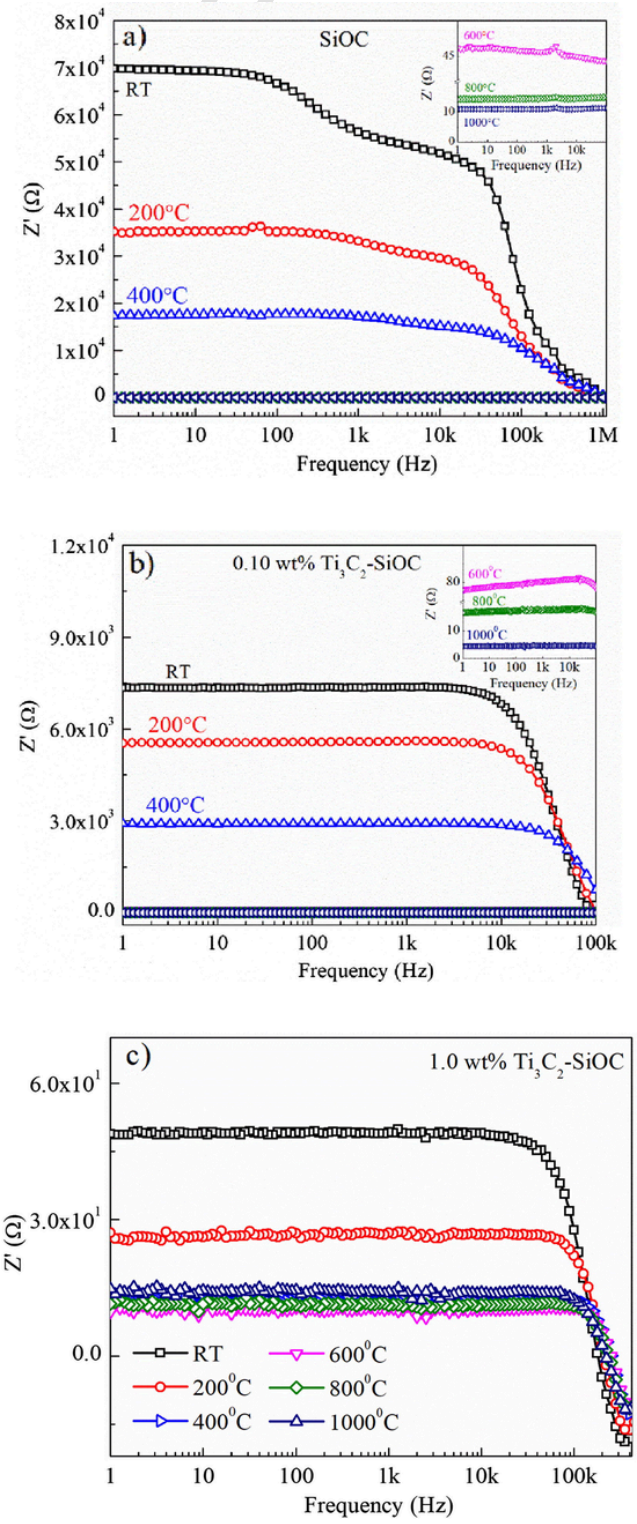

Fig. 11. Frequency dependence of the real impedance of a) pure SiOC, b) 0.1 wt% Ti_3C_2-SiOC, and c) 1.0 wt% Ti_3C_2-SiOC samples.

point for the SiOC sample at room temperature, which is indicative of charge carrier transport via two different paths (the SiOC matrix and carbon clusters), consistent with the Nyquist plot of the pure SiOC sample (Fig. 9a). However, increasing the measurement temperature results in only one inflection point, which implies thermal energy activation of high mobility carriers (electrons) to the conduction band. Additionally, simultaneous application of thermal and electric fields destabilizes the SiOC structure. For instance, structural ordering and modification of graphitic carbon clusters lead to formation of network-like structures. The thermal energy activates the Arrhenius conductivity by overcoming the potential barrier for the electrons to jump to the conduction band. Fig. 11a also shows that Z' decreases from an almost constant value to very low values at high frequencies, indicative of weakened capacitive characteristics.

Fig. 11b-c show the real impedance change with frequency for the Ti_3C_2-SiOC systems. As expected, from room temperature to 600 °C, the low frequency range exhibits only the DC resistance for the Ti_3C_2-SiOC systems. The respective DC resistance decreases with the Ti_3C_2 content. However, at high frequencies there is an inflection point for the 0.05 wt% Ti_3C_2-SiOC and 0.1 wt% Ti_3C_2-SiOC ceramics up to 600 °C. At higher measurement temperatures, the system exhibits a capacitance behavior, likely due to the contribution of the Ti_3C_2-SiOC-C interface. However, the temperature increase from 600 to 1000 °C does not cause any appreciable change in real impedance, which is indicative of DC resistance. A similar real impedance inflection point is seen for 1.0 wt% Ti_3C_2-SiOC up to 1000 °C, demonstrating the ohmic characteristic at high temperatures without the contribution of the Ti_3C_2-SiOC-C interfacial resistance. This means that high temperatures decrease the activation energy for the charge carrier jumping to the conduction band for 1.0 wt% Ti_3C_2-SiOC. Increase in the Ti_3C_2 content results in suppression of the capacitive behavior and the sample has more DC conducting characteristics.

Fig. 12 shows the changes of the imaginary impedance (Z'') with frequency for the pure SiOC, 0.1 wt% Ti_3C_2-SiOC, and 1.0 wt% Ti_3C_2-SiOC samples from room temperature to 1000 °C. The data for the 0.05 wt% Ti_3C_2-SiOC sample are similar to those of the other two Ti_3C_2-containing samples and omitted for brevity. Fig. 12a exhibits an increasing trend, a peak, and then a sudden drop with frequency. The frequency at which the slope changes is termed as characteristics frequency (f_c), indicating the dielectric relaxation process. The characteristic frequency is related to the relaxation time as:

$$\omega_c \tau_c = 2\pi f_c \tau_c = 1 \quad (3)$$

where ω_c and τ_c are characteristic angular frequency and relaxation time respectively. Fig. 12a shows that the characteristic frequency could not be evaluated. This observation is consistent with the Nyquist plot of the pure SiOC system, which indicates that the conduction is via two pathways, the SiOC matrix and the carbon clusters. For Ti_3C_2-SiOC, the imaginary component of the impedance as a function of frequency shows only one peak irrespective of the Ti_3C_2 content (Fig. 12b-c). The characteristic peak shifts to higher frequency with temperature, which suggests that more than one relaxation phenomenon is present. Fig. 12b shows that 0.10 wt% Ti_3C_2-SiOC has peaks at 39 $x10^3$ (room temperature), 106 $x10^3$ (200 °C), 299 $x10^3$ (400 °C), and 525$x10^3$ Hz (600 °C). Similarly, 1.0 wt% Ti_3C_2-SiOC has peaks at 138$x10^3$ (room temperature), 178$x10^3$ (200 °C), 252$x10^3$ (400 °C), and 261$x10^3$ Hz (600 °C). From 800 to 1000 °C, the corresponding peak decreases slightly to 259$x10^3$ and 212$x10^3$ Hz respectively. This could be due to more significant ohmic resistance of the SiOC matrix at high temperatures and also the contribution from the Ti_3C_2-SiOC-C interfacial resistance. It should be noted that the characteristic frequency is observed at all temperatures for 1.0 wt% Ti_3C_2-SiOC while for other samples the characteristic frequency is not observed at high temperatures.

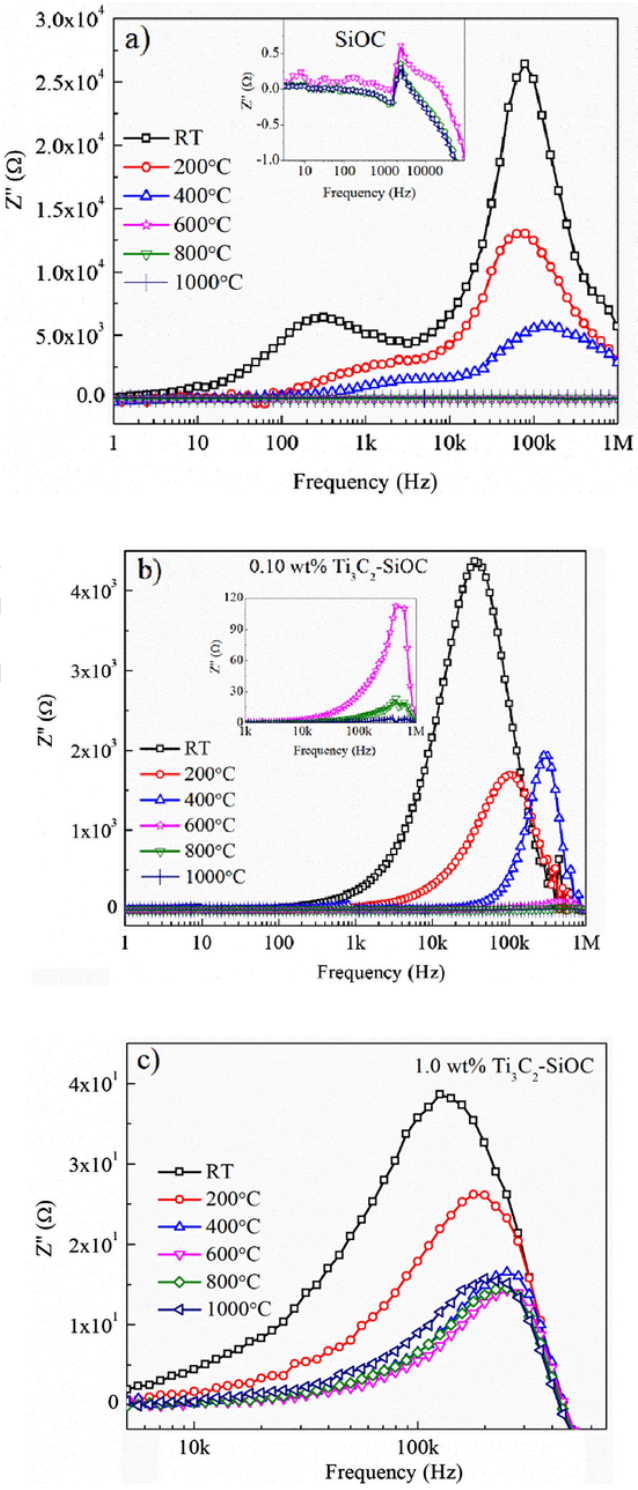

Fig. 12. Frequency dependence of the imaginary impedance of a) pure SiOC, b) 0.1 wt% Ti_3C_2-SiOC, and c) 1.0 wt% Ti_3C_2-SiOC samples.

4. Conclusions

In this study, MXene Ti_3C_2 has been exfoliated and then functionalized to prepare Ti_3C_2-SiOC composites. The Ti_3C_2 phase is preserved up to 1000 °C in the SiOC matrix and facilitates carbon cluster growth. Ti_3C_2 enhances the SiOC matrix electrical conductivity. The conductivity in the pure SiOC matrix occurs via both free carbon and the SiOC matrix while in the Ti_3C_2-SiOC samples Ti_3C_2 enables single percolation pathway. This work is the first to introduce Ti_3C_2 into the SiOC matrix.

The electrical behaviors of the Ti_3C_2-SiOC ceramics are first explained based on fundamental conduction mechanisms. These new systems demonstrate important application potentials from room temperature to as high as 1000 °C.

Declaration of Competing Interest

The authors declare that they have no known competing financial interests or personal relationships that could have appeared to influence the work reported in this paper.

Data availability

The raw data required to reproduce these findings are available to download from https://data.lib.vt.edu. The processed data required to reproduce these findings are available to download from https://data.lib.vt.edu.

Acknowledgement

This work was supported by Nation Science Foundation under grant no. CBET-2024546 and Air Force Office of Scientific Research under grant no. FA9550-22-1-0081.

References

[1] M. Alhabeb, K. Maleski, B. Anasori, P. Lelyukh, L. Clark, S. Sin, Y. Gogotsi, Chem. Mater. 29 (2017) 7633–7644.
[2] L. Verger, V. Natu, M. Carey, M.W. Barsoum, Trends in Chemistry 1 (2019) 656–669.
[3] B. Anasori, M.R. Lukatskaya, Y. Gogotsi, Nat. Rev. Mater. 2 (2017) 16098.
[4] V. Bayram, M. Ghidiu, J.J. Byun, S.D. Rawson, P. Yang, S.A. McDonald, M. Lindley, S. Fairclough, S.J. Haigh, P.J. Withers, M.W. Barsoum, I.A. Kinloch, S. Barg, ACS Applied Energy Materials 3 (2020) 411–422.
[5] H. Wang, Y. Wu, J. Zhang, G. Li, H. Huang, X. Zhang, Q. Jiang, Mater. Lett. 160 (2015) 537–540.
[6] P. Eklund, M. Beckers, U. Jansson, H. Högberg, L. Hultman, Thin Solid Films 518 (2010) 1851–1878.
[7] C. Vakifahmetoglu, D. Zeydanli, P. Colombo, Materials Science and Engineering R 106 (2016) 1–30.
[8] M. Scheffler, P. Greil, A. Berger, E. Pippel, J. Woltersdorf, Mater. Chem. Phys. 84 (2004) 131–139.
[9] P. Vallachira Warriam Sasikumar, E. Müller, P. Clement, J. Jang, E. Kakkava, G. Panusa, D. Psaltis, K. Maniura-Weber, M. Rottmar, J. Brugger, G. Blugan, ACS Applied Materials & Interfaces, 12 (2020) 17244-17253.
[10] R. Peña-Alonso, G. Mariotto, C. Gervais, F. Babonneau, G.D. Soraru, Chem. Mater. 19 (2007) 5694–5702.
[11] D. Erb, K. Lu, Mater. Chem. Phys. 209 (2018) 217–226.
[12] D. Erb, K. Lu, J. Am. Ceram. Soc. 101 (2018) 5378–5388.
[13] D. Erb, K. Lu, Mater. Chem. Phys. 237 (2019) 121844.
[14] J. Li, K. Lu, J. Am. Ceram. Soc. 98 (2015) 2357–2365.
[15] J. Li, K. Lu, T. Lin, F. Shen, J. Am. Ceram. Soc. 98 (2015) 1753–1761.
[16] J. Li, K.Y. Yu, Y. Chen, M. Song, H. Wang, M.A. Kirk, M. Li, X. Zhang, Nano Lett. 15 (2015) 2922–2927.
[17] K. Lu, D. Erb, Int. Mater. Rev. 63 (2018) 139–161.
[18] L.-H. Hu, R. Raj, J. Am. Ceram. Soc. 98 (2015) 1052–1055.
[19] M. Zaheer, G. Motz, R. Kempe, J. Mater. Chem. 21 (2011) 18825–18831.
[20] G. Glatz, T. Schmalz, T. Kraus, F. Haarmann, G. Motz, R. Kempe, Chemistry – A European Journal, 16 (2010) 4231-4238.
[21] F. Rosenburg, R. Riedel, R. Werthschützky, The State of Carbon and the Piezoresistive Effect in Silicon Oxycarbide Ceramics, Universitäts- und Landesbibliothek Darmstadt, 2018.
[22] Y. Cao, Electrical properties of polymer-derived silicoaluminum carboxide ceramics (SiAlCO) and their applications in micro-sensors, Electronic Theses and Dissertations, 2004-2019. 50932.
[23] K. Wang, B. Ma, Y. Wang, L. An, J. Am. Ceram. Soc. 96 (2013) 1363–1365.
[24] E. Bouillon, F. Langlais, R. Pailler, R. Naslain, F. Cruege, P.V. Huong, J.C. Sarthou, A. Delpuech, C. Laffon, P. Lagarde, M. Monthioux, A. Oberlin, J. Mater. Sci. 26 (1991) 1333–1345.
[25] K. Lu, D. Erb, M. Liu, J. Mater. Chem. C 4 (2016) 1829–1837.
[26] L. Wang, K. Lu, R. Ma, Appl. Phys. A 125 (2019) 395.
[27] K. Lu, D. Erb, M. Liu, J. Mater. Sci. 51 (2016) 10166–10177.
[28] S. Lai, J. Jeon, S.K. Jang, J. Xu, Y.J. Choi, J.-H. Park, E. Hwang, S. Lee, Nanoscale 7 (2015) 19390–19396.
[29] V. Borysiuk, V.N. Mochalin, MRS Commun. 9 (2019) 203–208.
[30] A. Lipatov, H. Lu, M. Alhabeb, B. Anasori, A. Gruverman, Y. Gogotsi, A. Sinitskii, Science Advances, 4 (2018) eaat0491.
[31] R. Li, L. Zhang, L. Shi, P. Wang, ACS Nano 11 (2017) 3752–3759.
[32] C. Moysan, R. Riedel, R. Harshe, T. Rouxel, F. Augereau, J. Eur. Ceram. Soc. 27 (2007) 397–403.
[33] T. Hu, J. Wang, H. Zhang, Z. Li, M. Hu, X. Wang, PCCP 17 (2015) 9997–10003.
[34] L.H. Li, Computational Matericals Science 124 (2016) 8–14.
[35] S. Hasegawa, H. Anbutsu, Y. Kurata, Philos. Mag. B 59 (1989) 365–375.
[36] Y. Jia, M.A.R. Chowdhury, C. Xu, J. Am. Ceram. Soc. 103 (2020) 6860–6868.
[37] V. Zólyomi, J. Koltai, J. Kürti, Physica Status Solidi (b) 248 (2011) 2435–2444.
[38] M.A. Pimenta, G. Dresselhaus, M.S. Dresselhaus, L.G. Cançado, A. Jorio, R. Saito, PCCP 9 (2007) 1276–1290.
[39] M.S. Dresselhaus, A. Jorio, A.G.S. Filho, R. Saito, Philosophical Transactions of the Royal Society A: Mathematical, Physical and Engineering Sciences 368 (2010) 5355–5377.
[40] A. Merlen, J.G. Buijnsters, C. Pardanaud, Coatings 7 (2017) 153.
[41] A.C. Ferrari, J. Robertson, Physical Review B 61 (2000) 14095–14107.
[42] L. Wang, K. Lu, J. Mater. Sci. 54 (2019) 6073–6087.
[43] S.K. Devendhar Singh, K. Bawane, Z. Hu, L. Yang, Y. Chen, L. Shao, K. Lu, Cerammics International, 48 (2022) 16063-16071.
[44] Z. Li, L. Wang, D. Sun, Y. Zhang, B. Liu, Q. Hu, A. Zhou, Mater. Sci. Eng., B 191 (2015) 33–40.
[45] F. Rosenburg, B. Balke, N. Nicoloso, R. Riedel, E. Ionescu, Molecules 25 (2020) 5919.
[46] N.A. Hegab, M.A. Afifi, H.E. Atyia, A.S. Farid, J. Alloy. Compd. 477 (2009) 925–930.
[47] K.O. Čajko, D.L. Sekulić, S. Lukić-Petrović, M.V. Šiljegović, D.M. Petrović, J. Mater. Sci.: Mater. Electron. 28 (2017) 120–128.
[48] Y. Wang, L. Zhang, W. Xu, T. Jiang, Y. Fan, D. Jiang, L. An, J. Am. Ceram. Soc. 91 (2008) 3971–3975.
[49] G. Lazar, K. Zellama, M. Clin, C. Godet, Appl. Phys. Lett. 85 (2004) 6176–6178.
[50] C. Godet, Philos. Mag. B 81 (2001) 205–222.